

# Structural diversity in iron(II) complexes of 2,6-di(pyrazol-1-yl)pyridine and 2,6-di(3-methylpyrazol-1-yl)pyridine†

Jérôme Elhaik, Colin A. Kilner and Malcolm A. Halcrow\*

Received 20th July 2005, Accepted 14th October 2005

First published as an Advance Article on the web 1st November 2005

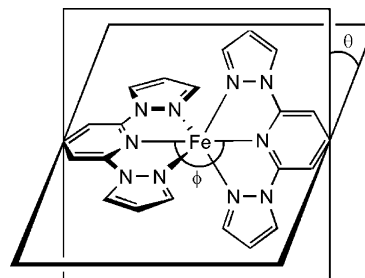
DOI: 10.1039/b510370c

The syntheses, magnetochemistry and crystallography of  $[\text{Fe}(\text{L}^1)_2]\text{I}_{0.5}[\text{I}_3]_{1.5}$  (**1**),  $[\text{Fe}(\text{L}^1)_2][\text{Co}(\text{C}_2\text{B}_9\text{H}_{11})_2]$  (**2**) and  $[\text{Fe}(\text{L}^2)_2][\text{SbF}_6]_2$  (**3**) ( $\text{L}^1 = 2,6\text{-di}(\text{pyrazol-1-yl})\text{pyridine}$ ;  $\text{L}^2 = 2,6\text{-di}(3\text{-methylpyrazol-1-yl})\text{pyridine}$ ) are described. Compounds **1** and **3** are high-spin between 5–300 K. For **1**, this reflects a novel variation of an angular Jahn–Teller distortion at the iron centre, which traps the molecule in its high-spin state. No such distortion is present in **3**; rather, the high-spin nature of this compound may reflect ligand conformational strain caused by an intermolecular steric contact in the crystal lattice. Compound **2** exhibits a gradual high  $\rightarrow$  low spin transition upon cooling with  $T_{\frac{1}{2}} = 318 \pm 3$  K, that is only 50% complete. This reflects the presence of two distinct, equally populated iron environments in the solid. One of these unique iron centres adopts the same angular structural distortion shown by **1** and so is trapped in its high-spin state, while the other, which undergoes the spin-crossover, has a more regular coordination geometry. In contrast with **3**, the solvated salts  $[\text{Fe}(\text{L}^2)_2][\text{BF}_4]_2 \cdot 4\text{CH}_3\text{CN}$  and  $[\text{Fe}(\text{L}^2)_2][\text{ClO}_4]_2 \cdot (\text{CH}_3)_2\text{CO}$  both undergo gradual thermal spin-transitions centred at  $175 \pm 3$  K.

## Introduction

We are continuing to study the spin-transition behaviour<sup>1</sup> of iron(II) complexes of 2,6-di(pyrazol-1-yl)pyridine<sup>2–10</sup> and 2,6-di(pyrazol-1-yl)pyrazine<sup>2,8,11–14</sup> ligands. The parent compound in this series is  $[\text{Fe}(\text{L}^1)_2]^{2+}$ , whose  $\text{BF}_4^-$  salt undergoes an abrupt spin-transition at 261 K.<sup>3–5,8</sup> In contrast the  $\text{ClO}_4^-$ ,  $\text{PF}_6^-$  and  $\text{SbF}_6^-$  salts of this material do not undergo spin-crossover, remaining fully high-spin between 5–300 K. That reflects their adoption of an unusual angular structural distortion, from the idealised  $D_{2d}$  symmetry expected with this ligand set towards  $C_2$  symmetry.<sup>4,10</sup> This is a result of Jahn–Teller splitting of the  $^5\text{E}$  high-spin ground state (in the  $D_{2d}$  point group), and is promoted in compounds of tridentate ligands with narrow bite angles like  $\text{L}^1$ .<sup>4</sup> The distortion can be characterised by two angles: a rotation of one ligand about the Fe ion, so that the *trans*-N{pyridine}–Fe–N{pyridine} angle ( $\phi$  in Scheme 1)  $< 180^\circ$ ; and, a twist of the plane of one ligand relative to the other about the N{pyridine}–Fe–N{pyridine} vector (*i.e.*  $\theta < 90^\circ$ , Scheme 1). These two components usually occur together in a distorted  $[\text{Fe}(\text{L}^1)_2]^{2+}$  salt and related compounds, typically yielding  $\phi \approx 155^\circ$  and  $\theta \approx 60^\circ$ .<sup>9,10,14</sup> However one example is known that exhibits the ‘twist’ component of the distortion only, possibly for steric reasons.<sup>10</sup> Comparison of all these compounds has suggested that the zero-field splitting of the high-spin species can be used as a qualitative indicator of the presence of the

‘rotation’ component of the structural distortion. Undistorted high-spin complexes of this type exhibit a zero-field splitting parameter  $|D| \approx 12 \text{ cm}^{-1}$ , while compounds with  $\phi < 180^\circ$  commonly show  $3 \leq |D| \leq 8 \text{ cm}^{-1}$ .<sup>10</sup>



**Scheme 1** The angles referred to in the discussion of the Jahn–Teller distortion in high-spin  $[\text{Fe}(\text{L}^1)_2]^{2+}$ .

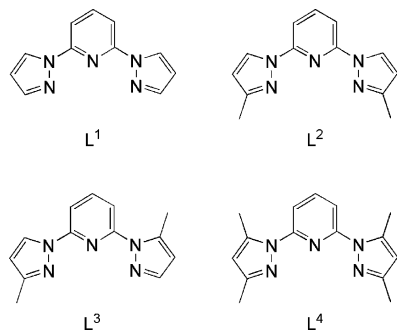
The reluctance of  $[\text{Fe}(\text{L}^1)_2]^{2+}$  salts to undergo thermal spin-transitions contrasts with the  $[\text{FeL}_2]^{2+}$  complex of 2,6-di(pyrazol-3-yl)pyridine, which is a regioisomer of  $\text{L}^1$ .<sup>2</sup> A large number of hydrated and anhydrous salts of the latter complex dication have been isolated, many of which undergo thermal spin-transitions exhibiting novel solid state physics.<sup>15</sup> For this reason, we have continued to prepare new salts of  $[\text{Fe}(\text{L}^1)_2]^{2+}$ , which might also show novel spin-crossover behaviour. We report here the synthesis, and crystallographic and magnetochemical characterisation of two such compounds:  $[\text{Fe}(\text{L}^1)_2]\text{I}_{0.5}[\text{I}_3]_{1.5}$  (**1**) and  $[\text{Fe}(\text{L}^1)_2][\text{Co}(\text{C}_2\text{B}_9\text{H}_{11})_2]$  (**2**). We also describe the first complex salts of the related ligand  $\text{L}^2$ , including  $[\text{Fe}(\text{L}^2)_2][\text{SbF}_6]_2$  (**3**). Taken together, **1–3** further extend the unusual structural and magnetochemical complexity observed in this metal/ligand system.

School of Chemistry, University of Leeds, Woodhouse Lane, Leeds, UK LS2 9JT. E-mail: M.A.Halcrow@chem.leeds.ac.uk

† Electronic supplementary information (ESI) available: Experimental details, figure and tables of bond lengths and angles from the crystal structures of the solvate salts  $[\text{Fe}(\text{L}^2)_2][\text{BF}_4]_2 \cdot 4\text{CH}_3\text{CN}$  and  $[\text{Fe}(\text{L}^2)_2][\text{ClO}_4]_2 \cdot (\text{CH}_3)_2\text{CO}$  at four temperatures; a plot of the variation of Fe–N bond lengths in these compounds with temperature; and, a table of C–H...I hydrogen bonding parameters in **1**. See DOI: 10.1039/b510370c

## Results and discussion

No complexes of  $L^2$  have been described before, although its synthesis by the reaction of deprotonated 3{5}-methylpyrazole with 0.5 equiv. of 2,6-dibromopyridine has been reported by two groups.<sup>16,17</sup> Both literature procedures gave a mixture of  $L^2$  and its 3,5''-dimethyl regioisomer  $L^3$ , which could not be separated. We have found that, although  $L^2$  and  $L^3$  elute at almost identical rates by flash chromatography, a low yield of pure  $L^2$  can be separated by careful elution of the crude product mixture down a silica column in 3 : 1 pentane/diethyl ether. The  $^1\text{H}$  NMR spectrum of pure  $L^2$  matches that previously reported for this compound.<sup>17</sup>



Treatment of  $\text{FeI}_2 \cdot 4\text{H}_2\text{O}$  with 2 equiv. of  $L^1$  in MeOH at room temperature gives an orange solution, which yields the orange powder  $[\text{FeI}_2L^1]$  following concentration *in vacuo* and slow addition of  $\text{Et}_2\text{O}$ . However, performing the reaction under reflux for 2 h in air, followed by the same work-up, affords approximately equal amounts of  $[\text{FeI}_2L^1]$  and a new, brown crystalline compound  $[\text{Fe}(L^2)_2]_{0.5}[\text{I}_3]_{1.5}$  (**1**). The  $\text{I}_3^-$  content in **1** probably arises from aerobic oxidation of iodide under the more forcing reaction conditions. These two products could be separated by decantation, allowing **1** to be fully characterised as described below. Although we have not obtained a crystal structure of  $[\text{FeI}_2L^1]$ , it presumably adopts a five-coordinate geometry analogous to that shown by  $[\text{FeCl}_2L^4]$  in the crystal.<sup>18</sup> The ES mass spectra of **1** and  $[\text{FeI}_2L^1]$  in MeCN are almost identical, each containing the strong molecular ions  $[\text{Fe}_2\text{I}_3(L^1)_2]^+$  ( $m/z$  915),  $[\text{FeI}(L^1)]^+$  (394),  $[\text{FeI}(L^1)_2]^{2+}$  (302) and  $[\text{Fe}(L^1)_2]^{2+}$  (239). This implies that the  $L^1$  ligands in **1** are partially displaced by the iodide ions in this solvent, which explains why freshly crystallised **1** is always contaminated with  $[\text{FeI}_2L^1]$ . Similar reactions using  $\text{FeCl}_2 \cdot 4\text{H}_2\text{O}$  yielded  $[\text{FeCl}_2L^1]$ <sup>19</sup> as the only isolable product.

The salt  $[\text{Fe}(L^1)_2][\text{Co}(\text{C}_2\text{B}_9\text{H}_{11})_2]$  (**2**) was obtained by reaction of  $\text{FeCl}_2 \cdot 4\text{H}_2\text{O}$  with 2 equiv. of  $L^1$  and excess  $\text{Ag}[\text{Co}(\text{C}_2\text{B}_9\text{H}_{11})_2]$  in refluxing  $\text{CH}_3\text{NO}_2$ . Diffusion of  $\text{Et}_2\text{O}$  vapour into the filtered, orange solution affords air-sensitive orange needles of the  $\text{CH}_3\text{NO}_2$  solvate of **2**. Microanalysis and  $^1\text{H}$  NMR spectroscopy both imply that this solvent content is lost upon drying *in vacuo*, and magnetochemical measurements were carried out using this dried material. Finally,  $[\text{Fe}(L^2)_2][\text{SbF}_6]_2$  (**3**) was obtained by reaction of  $\text{FeCl}_2 \cdot 4\text{H}_2\text{O}$ ,  $L^2$  and  $\text{AgSbF}_6$  in a 1 : 2 : 2 molar ratio, under the same conditions used for **2**. Diffusion of  $\text{Et}_2\text{O}$  vapour into a solution of **3** in acetone yielded large mustard yellow, solvent-free crystals of the compound.

Variable temperature susceptibility measurements were carried out on **1–3**.  $\chi_M T$  for **1** remains constant at  $3.3 \text{ cm}^3 \text{ mol}^{-1} \text{ K}$  between 30–300 K, before decreasing slightly at lower temperatures (Fig. 1).

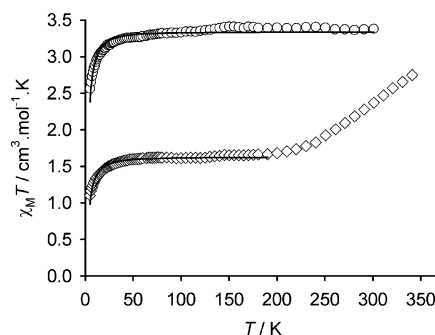


**Fig. 1** Variable temperature susceptibility data for **1** (○) and **2** (◇). The lines are the fits of these data to the expression for the zero-field splitting of the iron centre. See text for more details.

This demonstrates that, despite its brown colouration (which is normally exhibited by low-spin  $[\text{Fe}(L^1)_2]^{2+}$  compounds<sup>3–7,11,13,14</sup>), **1** is high-spin over this entire temperature range. The low-temperature decrease in  $\chi_M T$  for **1** results from zero-field splitting of the  $^5\text{E}$  high-spin manifold.<sup>20,21</sup> These data were modelled to afford  $g = 2.109(2)$  and  $|D| = 7.6(2) \text{ cm}^{-1}$ . This value of  $|D|$  implies that **1** adopts the angular structural distortion found in several other  $[\text{Fe}(L^1)_2]^{2+}$  salts,<sup>10</sup> which was confirmed by the crystallographic study described below. The magnetic data for **3** (not shown in Fig. 1) are very similar to those of **1**, and yielded the parameters  $g = 2.140(4)$  and  $|D| = 9.9(3) \text{ cm}^{-1}$ . This value of  $|D|$  is intermediate between those previously observed for complexes in this series with regular and distorted structures.<sup>10</sup> That **3** should remain high-spin on cooling was unexpected, since we have crystallographically characterised two other solvated salts of  $[\text{Fe}(L^2)_2]^{2+}$  that do undergo gradual thermal spin-transitions, both centred at  $175 \pm 3 \text{ K}$  (ESI†).

In contrast,  $\chi_M T$  for **2** decreases steadily upon cooling, from  $2.7 \text{ cm}^3 \text{ mol}^{-1} \text{ K}$  at 340 K to  $1.7 \text{ cm}^3 \text{ mol}^{-1} \text{ K}$  at 220 K, but remains at  $1.6\text{--}1.7 \text{ cm}^3 \text{ mol}^{-1} \text{ K}$  upon further cooling before showing a small decrease below 50 K as before. If  $\chi_M T$  of the fully high-spin sample is estimated to be  $3.3\text{--}3.4 \text{ cm}^3 \text{ mol}^{-1} \text{ K}$ , this behaviour implies that approximately 50% of the iron centres in the material undergo a gradual high  $\rightarrow$  low spin transition centred at  $T_{1/2} = 318 \pm 3 \text{ K}$ , while the remaining iron content remains high-spin at all temperatures. Incomplete spin-transitions of this type can originate through several different effects. Most simply, they can reflect the existence of more than one type of magnetically inequivalent iron environment in the sample.<sup>22</sup> Alternatively, they may be a consequence of a crystallographic phase change during spin-crossover;<sup>23</sup> of intermolecular steric interactions;<sup>9</sup> of lattice strain induced by structural changes occurring during spin-crossover;<sup>24</sup> or, of an unusually large kinetic barrier to the transition.<sup>25</sup> The crystallographic investigation of **2** described below shows that the first explanation is relevant here. Fitting the  $\chi_M T$  vs.  $T$  data for **2** below 200 K yields parameters  $g = 2.080(3)$  and  $|D| = 10.2(2) \text{ cm}^{-1}$ , assuming that 50% of the material is high-spin at these temperatures. As for **3**, this value of  $|D|$  is again intermediate between the values expected if the high-spin fraction of this compound has a distorted or undistorted six-coordinate geometry.

The asymmetric unit of crystalline **1** contains one half-occupied  $\text{I}^-$  anion and three half-occupied  $\text{I}_3^-$  ions all lying on crystallographic  $C_2$  axes; and a complex dication occupying a general

**Table 1** Selected bond lengths (Å) and angles (°) for  $[\text{Fe}(\text{L}^1)_2]\text{I}_{0.5}[\text{I}_3]_{1.5}$  (**1**) and  $[\text{Fe}(\text{L}^1)_2][\text{Co}(\text{C}_2\text{B}_9\text{H}_{11})_2]_2 \cdot \text{CH}_3\text{NO}_2$  (**2**· $\text{CH}_3\text{NO}_2$ ). The angles ' $\phi$ ' and ' $\theta$ ' are defined in Scheme 1

	<b>1</b>	<b>2</b> at 300 K		<b>2</b> at 150 K	
		Molecule A	Molecule B	Molecule A	Molecule B
Fe(1)–N(2)	2.141(4)	1.981(5)	2.127(5)	1.917(7)	2.163(8)
Fe(1)–N(9)	2.181(4)	1.962(6)	2.167(6)	1.996(8)	2.202(9)
Fe(1)–N(14)	2.185(5)	2.030(4)	2.158(6)	1.983(7)	2.172(8)
Fe(1)–N(18)	2.159(4)	1.975(4)	2.131(3)	1.916(7)	2.129(7)
Fe(1)–N(25)	2.171(5)	2.031(5)	2.173(4)	1.958(8)	2.180(7)
Fe(1)–N(30)	2.231(5)	2.035(6)	2.210(4)	1.980(8)	2.231(8)
N(2)–Fe(1)–N(9)	73.22(16)	80.9(3)	74.5(3)	79.6(4)	74.6(3)
N(2)–Fe(1)–N(14)	72.45(16)	77.87(19)	72.6(3)	80.4(3)	71.7(3)
N(2)–Fe(1)–N(18) ( $\phi$ )	155.97(16)	175.7(2)	163.11(15)	178.3(3)	159.6(3)
N(2)–Fe(1)–N(25)	129.20(16)	99.83(18)	122.94(16)	98.5(3)	124.7(3)
N(2)–Fe(1)–N(30)	86.29(16)	104.4(2)	90.03(16)	101.6(3)	88.1(3)
N(9)–Fe(1)–N(14)	142.24(17)	158.4(2)	146.2(2)	159.9(3)	145.3(3)
N(9)–Fe(1)–N(18)	115.31(16)	102.4(2)	108.27(19)	101.6(3)	112.3(3)
N(9)–Fe(1)–N(25)	99.32(16)	96.2(2)	99.42(19)	93.9(3)	100.4(3)
N(9)–Fe(1)–N(30)	90.82(16)	89.0(2)	93.42(18)	90.0(3)	92.4(3)
N(14)–Fe(1)–N(18)	102.44(16)	99.08(17)	105.41(19)	98.5(3)	102.2(3)
N(14)–Fe(1)–N(25)	90.41(17)	91.30(18)	92.2(2)	90.8(3)	92.2(3)
N(14)–Fe(1)–N(30)	102.14(17)	92.5(2)	93.92(17)	92.3(3)	94.3(3)
N(18)–Fe(1)–N(25)	73.31(16)	77.08(19)	73.57(15)	80.2(3)	74.1(3)
N(18)–Fe(1)–N(30)	71.62(16)	78.6(2)	73.27(14)	79.7(3)	72.8(3)
N(25)–Fe(1)–N(30)	144.51(16)	155.7(2)	146.72(15)	160.0(3)	146.9(3)
$\theta$	89.92(5)	86.04(7)	86.12(6)	87.42(10)	87.03(9)

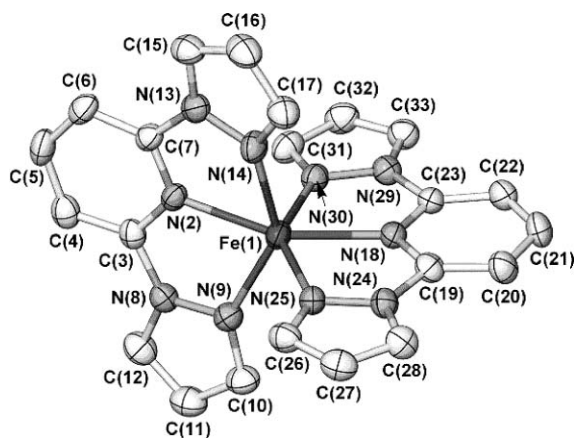


**Fig. 2** View of the complex dication in the crystal structure of  $[\text{Fe}(\text{L}^1)_2]\text{I}_{0.5}[\text{I}_3]_{1.5}$  (**1**), showing the atom numbering scheme employed. All H atoms have been omitted, and thermal ellipsoids are at the 50% probability level.

position (Fig. 2, Table 1). The six-coordinate iron centre is clearly high-spin from its Fe–N bond lengths [2.141(4)–2.231(5) Å] and average  $\text{L}^1$  bite angle [72.9(3)°].<sup>3–5,8–14</sup> However, as predicted by the magnetic data, the complex dication deviates strongly from the ‘ideal’  $D_{2d}$ -symmetric geometry expected with this ligand set. Interestingly, only the ‘rotation’ distortion is observed with  $\phi = 155.97(16)^\circ$  (Scheme 1); the ‘twist’ distortion is not present since the two  $\text{L}^1$  ligands in the molecule are perpendicular to within experimental error [ $\theta = 89.92(5)^\circ$ ]. This is the first time that the ‘rotation’ distortion has been observed in isolation in this class of compound. Concomitant with this distortion, Fe(1) protrudes out of the least squares planes of the two ligands, by 0.406(2) Å [ligand N(2)–C(17)] and 0.180(3) Å [N(18)–C(33)].

The cations of **1** aggregate into chains parallel to the lattice  $c$  direction, through a long  $\pi$ – $\pi$  interaction between pyrazole rings N(13)–C(17) and N(8<sup>i</sup>)–C(12<sup>i</sup>) (symmetry code  $i: x, 2 - y, -\frac{1}{2} + z$ ). These groups are 3.40(2) Å apart, and have a dihedral angle between them of 4.8(5)°. The  $\text{I}_3^-$  ions in **1** are aligned almost coparallel with each other, in rectangular channels along the crystallographic [101] vector (Fig. 3). The channels are formed

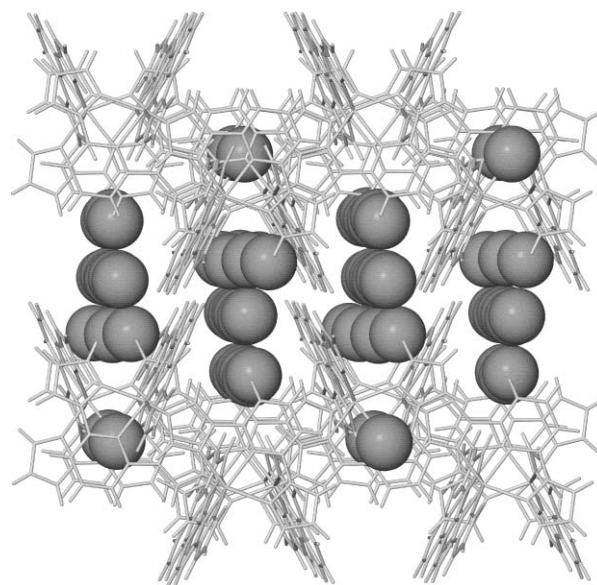


**Fig. 3** Partial packing diagram of  $[\text{Fe}(\text{L}^1)_2]\text{I}_{0.5}[\text{I}_3]_{1.5}$  (**1**), showing the channels occupied by the  $\text{I}_3^-$  ions. The I atoms are plotted with their van der Waals radii, while the complex dications are de-emphasised. For clarity, only one orientation of the disordered  $\text{I}_3^-$  ion is shown. The view is perpendicular to the [101] crystal vector, with the unit cell  $b$  direction vertical.

from cavities of approximate dimensions  $3.4 \times 9.2 \text{ \AA}$ , which contain two of the  $\text{I}_3^-$  environments, linked by constrictions of *ca.*  $3.2 \times 4.6 \text{ \AA}$  that hold the third one. The  $\text{I}^-$  ions occupy pockets in the lattice that cap one narrow side of the constrictions. All these anions are held in place by  $\text{C-H} \cdots \text{I}$  hydrogen bonds (ESI†). The closest interatomic contacts between neighbouring  $\text{I}_3^-$  anions are  $4.3\text{--}4.4 \text{ \AA}$ , essentially equal to the sum of the van der Waals radii of two iodine atoms ( $4.3 \text{ \AA}^{26}$ ). Hence there are no significant bonding interactions between the anions in the lattice, which supports the formulation of the structure as containing discrete  $\text{I}^-$  and  $\text{I}_3^-$  centres, rather than longer polyiodide chains.<sup>27</sup>

Crystals of  $2\text{-CH}_3\text{NO}_2$  are weak diffractors, particularly at room temperature, which may reflect their needle morphology and/or disorder caused by the mixture of spin-states they contain. Despite this caveat, the spin-states and stereochemistries of the iron centres at the temperatures of measurement (150 and 300 K) are unambiguous. The asymmetric unit of  $2\text{-CH}_3\text{NO}_2$  contains two formula units, with two iron centres that are structurally very different (Fig. 4, Table 1). Molecule A has a nearly regular  $D_{2d}$ -symmetric geometry, with Fe–N bond lengths [ $1.916(7)\text{--}1.996(8) \text{ \AA}$ ] and average  $L^1$  bite angle [ $80.0(7)^\circ$ ] at 150 K that are consistent with a fully

low-spin structure.<sup>3–7,11,13,14</sup> At 300 K, five of the six Fe–N distances have increased from their low-temperature value, by between 6 and 8  $\mu\text{s}$ . That implies this crystal site now contains a mixture of high- and low-spin molecules, albeit with the low-spin form still predominating. In contrast, molecule B shows a  $C_2$ -distorted geometry that closely resembles that in **1**. As in **1**, only a significant ‘rotation’ component of the Jahn–Teller distortion is present in the molecule [ $\phi = 159.6(3)$ ,  $\theta = 87.03(9)^\circ$ ] at 150 K]. As expected, the Fe–N distances and ligand bite angle at both temperatures indicate that this site is fully high-spin [at 300 K, these are  $2.127(5)\text{--}2.210(4) \text{ \AA}$  and  $73.5(5)^\circ$ ; at 150 K,  $2.129(7)\text{--}2.231(8) \text{ \AA}$  and  $73.3(6)^\circ$ ]. Interestingly, bonds Fe(1B)–N(2B) and Fe(1B)–N(9B) appear to be shorter at 300 K than at 150 K, although these differences are of marginal statistical significance at  $<4 \text{ \mu s}$ . The structure of molecule B is further distorted by a steric contact between C(27B) and a cobalticarborene B–H group (not shown in Fig. 4), which forces pyrazole ring N(24B)–C(28B) to bend out of the plane of the rest of that  $L^1$  ligand, by  $14.6(4)^\circ$  at 150 K. The open face in molecule B created by the rotation distortion is filled by another anion, lying above and parallel to the ligand N(2B)–C(27B) (not shown in Fig. 4).

This compound is the first example of this class of iron(II) complex to contain co-crystallised  $C_2$ -distorted and undistorted molecules, which explains its incomplete thermal spin-transition. Molecule A, which is low-spin at 150 K but in a mixture of spin states at 300 K, undergoes a gradual transition to its high-spin form at higher temperatures. The bond lengths at Fe(1A) imply that this transition is  $<50\%$  complete at 300 K, consistent with the magnetic data (Fig. 1). Molecule B, in contrast, is trapped in its high-spin state by its angular Jahn–Teller distortion<sup>4</sup> and remains high-spin at all temperatures.

The complex dications in  $2\text{-CH}_3\text{NO}_2$  are well-separated from each other. The only short intermolecular contacts between complex molecules are: a  $\pi\text{--}\pi$  interaction between pyrazole rings N(13A)–C(17A) and N(29B)–C(33B), which are separated by  $3.30(4) \text{ \AA}$  with a dihedral angle between them of  $0.5(4)^\circ$  at 150 K; and, a long  $\text{C-H} \cdots \pi$  contact of  $2.82 \text{ \AA}$  between C(32B)–H(32B) and the centroid of ring N(24A)–C(28A) (the van der Waals radii of an H atom and arene ring are 1.2 and  $1.7 \text{ \AA}$  respectively<sup>26</sup>). Importantly, molecule A interacts with its nearest neighbour of the same type (related by  $x, 1 + y, z$ ) through van der Waals interactions only. The lack of direct interactions between molecules A in the lattice is consistent with the gradual, non-cooperative spin-transition undergone by this compound. In addition to these inter-cation interactions, there are several intermolecular  $\text{C-H} \cdots \text{H-B}$  contacts of  $2.1\text{--}2.3 \text{ \AA}$  between the  $L^1$  ligands and cobalticarborene anions in the lattice, and  $\text{C-H} \cdots \text{O}$  contacts of  $2.4\text{--}2.5 \text{ \AA}$  between the ligands and solvent.

Consistent with its magnetic behaviour, the Fe–N bond lengths [ $2.125(3)\text{--}2.214(3) \text{ \AA}$ ] and average ligand bite angle [ $73.7(2)^\circ$ ] in **3** at 150 K indicate that this compound has a high-spin structure (Fig. 5, Table 2). Unlike the other high-spin compounds in this study, however, this complex has a near-regular  $D_{2d}$ -symmetric geometry, with the distortion angles  $\phi$  and  $\theta$  (Scheme 1) both being close to their ideal values (Table 2). These parameters are very similar to those exhibited by the high-spin forms of the solvate salts  $[\text{Fe}(L^2)]_2[\text{BF}_4]_2 \cdot 4\text{CH}_3\text{CN}$  and  $[\text{Fe}(L^2)]_2[\text{ClO}_4]_2 \cdot (\text{CH}_3)_2\text{CO}$ , which do undergo a thermal spin-transition upon cooling (ESI†). Hence the high-spin nature of **3** cannot reflect either a structural

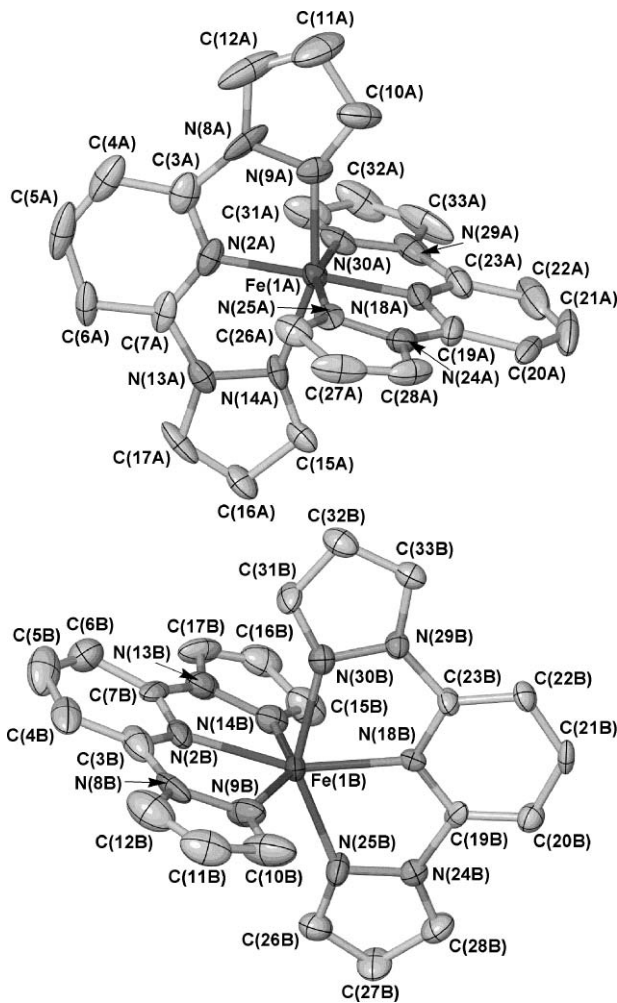


**Fig. 4** View of the two independent complex dications in the crystal structure of  $[\text{Fe}(L^1)]_2[\text{Co}(\text{C}_2\text{B}_9\text{H}_{11})_2] \cdot \text{CH}_3\text{NO}_2$  ( $2\text{-CH}_3\text{NO}_2$ ) at 150 K, showing the atom numbering scheme employed. All H atoms have been omitted, and thermal ellipsoids are at the 50% probability level.

**Table 2** Selected bond lengths (Å) and angles (°) for  $[\text{Fe}(\text{L}^2)_2][\text{SbF}_6]_2$  (**3**). The angles ' $\phi$ ' and ' $\theta$ ' are defined in Scheme 1

Fe(1)–N(2)	2.125(3)	Fe(1)–N(20)	2.129(3)
Fe(1)–N(9)	2.182(3)	Fe(1)–N(27)	2.183(3)
Fe(1)–N(15)	2.169(3)	Fe(1)–N(33)	2.214(3)
N(2)–Fe(1)–N(9)	73.63(11)	N(9)–Fe(1)–N(33)	98.28(11)
N(2)–Fe(1)–N(15)	73.94(11)	N(15)–Fe(1)–N(20)	106.15(11)
N(2)–Fe(1)–N(20) ( $\phi$ )	177.95(11)	N(15)–Fe(1)–N(27)	91.94(11)
N(2)–Fe(1)–N(27)	108.67(11)	N(15)–Fe(1)–N(33)	89.87(12)
N(2)–Fe(1)–N(33)	104.14(11)	N(20)–Fe(1)–N(27)	73.38(11)
N(9)–Fe(1)–N(15)	147.56(11)	N(20)–Fe(1)–N(33)	73.83(11)
N(9)–Fe(1)–N(20)	106.28(11)	N(27)–Fe(1)–N(33)	146.32(11)
N(9)–Fe(1)–N(27)	98.03(11)		
$\theta$	85.84(10)		

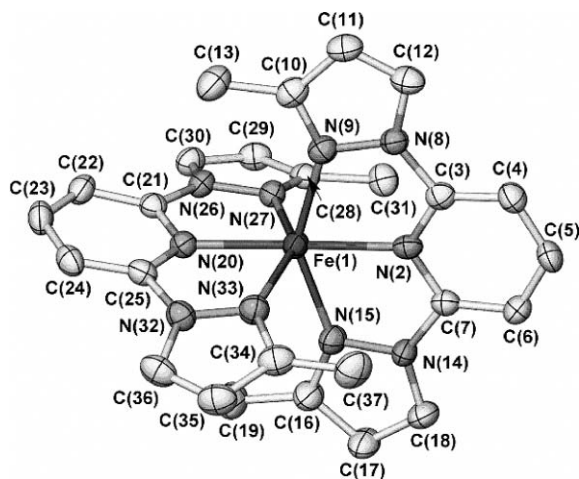


**Fig. 5** View of the complex dication in the crystal structure of  $[\text{Fe}(\text{L}^2)_2][\text{SbF}_6]_2$  (**3**), showing the atom numbering scheme employed. All H atoms have been omitted, and thermal ellipsoids are at the 50% probability level.

distortion of the iron coordination sphere, or intramolecular steric contacts involving the ligand methyl groups (as is observed in analogous compounds with larger pyrazole substituents<sup>10</sup>). Rather, we tentatively attribute the fact that **3** is trapped in its high-spin state to the very twisted conformation exhibited by ligand N(20)–C(37), which deviates strongly from planarity (Fig. 6). The dihedral angles between the least squares planes of pyridine ring N(20)–C(25) and pyrazole rings N(26)–C(30) and N(32)–C(36) are 17.2(2) and 21.8(2)°, respectively. This distortion most likely reflects intermolecular steric contacts between C(18<sup>ii</sup>)–H(18<sup>ii</sup>) and C(35) (2.72 Å) and C(36) (2.64 Å) (symmetry code ii:  $x, -\frac{1}{2} - y, \frac{1}{2} + z$ ). These distances are significantly shorter than the sum of the radii of an H atom and aryl group (1.2 and 1.7 Å), and are positioned to displace pyrazole ring N(32)–C(36) out of the meridional plane of the complex (Fig. 6). We propose that its strained conformation introduces additional rigidity into this L<sup>2</sup> ligand, disavouring the structural rearrangement required during a spin-transition. For comparison the equivalent inter-heterocycle dihedral angles in the other ligand, N(2)–C(19), are 7.01(11) and 1.72(14)°. There are no other noteworthy intermolecular interactions in the crystal lattice of **3**.

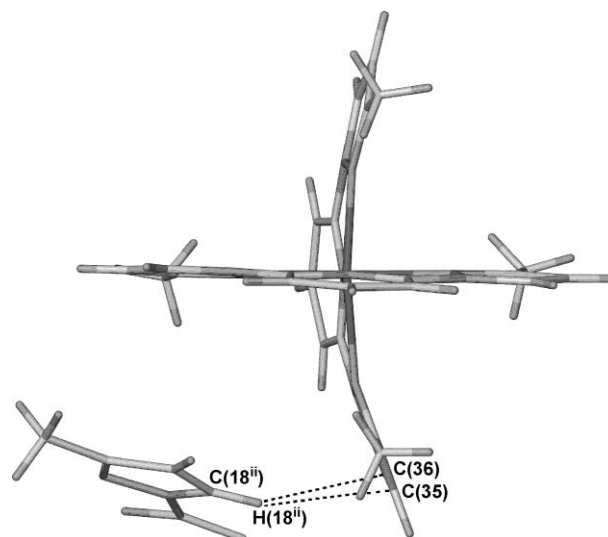


**Fig. 6** Alternative view of the complex dication in the crystal structure of  $[\text{Fe}(\text{L}^2)_2][\text{SbF}_6]_2$  (**3**), emphasising the conformational distortion in ligand N(20)–C(37), which is vertical and to the rear. The intermolecular steric contact that causes this distortion is also shown. All atoms have arbitrary radii. Symmetry code ii:  $x, -\frac{1}{2} - y, \frac{1}{2} + z$ .

## Conclusion

We have shown previously that a high-spin state can be imposed onto an iron(II)–2,6-di(pyrazol-1-yl)pyridine complex through the angular Jahn–Teller distortion<sup>4,9,10,14</sup> or, when this is not present, through intramolecular steric interactions between the two ligands in the molecule.<sup>6,10</sup> This study has extended our knowledge of these phenomena in three ways. First, **1** and molecule B of **2** are the first compounds to show purely the ‘rotation’ component of the structural distortion (*i.e.*  $\phi < 180$ ,  $\theta \approx 90^\circ$ ). We have previously isolated one complex that undergoes only the ‘twist’ component ( $\phi = 180$ ,  $\theta < 90^\circ$ ), using a sterically bulky 2,6-di(pyrazol-1-yl)pyridine derivative.<sup>10</sup> Since **1** and **2** do not contain bulky substituents, this work confirms that the two components of the Jahn–Teller distortion in this system can occur independently of one another even in the absence of steric effects. Compound **2** is also important as the first material to contain co-crystallised distorted and undistorted molecules of the same complex. This confirms that the different forms of the same compound can co-exist in the solid and, presumably, also in solution. The plethora of different stereochemistries observed in salts of  $[\text{Fe}(\text{L}^1)_2]^{2+}$  simply reflects which one crystallises preferentially from this mixture of structures in solution.

The novel structures of **1** and **2** have allowed us to extend our magnetostructural correlation for the angular distortion in these compounds (Fig. 7). We previously suggested that the ‘rotation’ component was the dominant factor in the reduced zero-field splittings  $|D|$  of 3–8 cm<sup>−1</sup> shown by the distorted structures.<sup>10</sup> Fig. 7 supports that contention, in that compounds showing only the ‘rotation’ distortion exhibit reduced values of  $|D|$ , while the example exhibiting only the ‘twist’ component does not. However, it is also clear that the lowest values of  $|D|$  are exhibited by those complexes adopting reduced values of *both* distortion angles. Fig. 7 demonstrates that a small zero-field splitting of 3–5 cm<sup>−1</sup> should be diagnostic for a structure with  $\phi \approx 155^\circ$  and  $\theta \approx 60^\circ$ .

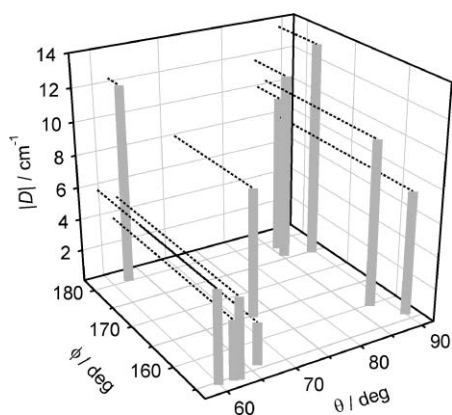


**Fig. 7** Correlation of the structural distortion, as defined in Scheme 1, with the zero-field splitting parameters shown by the high-spin iron centres in **1–3** and the compounds in refs. 4, 10 and 14. Errors on  $|D|$  in this plot are  $\pm 0.2$ – $0.5$   $\text{cm}^{-1}$ .

However, intermediate values of  $7 \leq |D| \leq 10$   $\text{cm}^{-1}$  cannot be simply assigned to a particular structural type in this system, and should be interpreted with care.

Finally, compound **3** introduces a new way in which this class of iron(II) complex can become trapped in a high-spin state. Rather than showing a distorted metal coordination sphere, **3** exhibits a severe conformational distortion at one of its  $L^2$  ligands that is induced by an intermolecular steric contact. The plethora of structures adopted by high-spin iron(II)–2,6-di(pyrazol-1-yl)pyridine complexes has not been seen in any other stereochemically related six-coordinate compounds, and will make the controlled synthesis of new spin-transition materials based on this motif a particular challenge.

## Experimental

Unless otherwise stated, all manipulations were carried out in air using reagent grade solvents, except that bis(2-methoxyethyl) ether was dried over sodium before use. 2,6-Di(pyrazol-1-yl)pyridine ( $L^1$ )<sup>16</sup> and  $\text{Ag}[\text{Co}(\text{C}_2\text{B}_9\text{H}_{11})_2]^{28}$  were prepared by the literature procedures, while all other reagents were used as supplied. Synthetic, analytical and crystallographic data for  $[\text{Fe}(\text{L}^2)_2][\text{BF}_4]_2 \cdot 4\text{CH}_3\text{CN}$  and  $[\text{Fe}(\text{L}^2)_2][\text{ClO}_4]_2 \cdot (\text{CH}_3)_2\text{CO}$  are given in the ESI<sup>†</sup>. The solution phase NMR, UV/vis and susceptibility data from  $[\text{Fe}(\text{L}^1)_2]^{2+}$  (as  $[\text{Fe}(\text{L}^1)_2][\text{BF}_4]_2$ ) have been reported previously.<sup>4</sup>

### Synthesis of 2,6-di(3-methylpyrazol-1-yl)pyridine ( $L^2$ )

A mixture of 3{5}-methylpyrazole (3.7 g,  $4.6 \times 10^{-2}$  mol) and potassium hydride (1.8 g,  $4.6 \times 10^{-2}$  mol) in bis(2-methoxyethyl) ether (150  $\text{cm}^3$ ) under  $\text{N}_2$  was stirred for 1 h, affording a white suspension. Solid 2,6-dibromopyridine (5.32 g,  $2.2 \times 10^{-2}$  mol) was added to the mixture, which was then stirred at 130 °C for 5 days. The cooled mixture was quenched with water (300  $\text{cm}^3$ ), yielding a white precipitate of the crude product which was isolated and dried over phosphorous pentoxide. Flash silica chromatography (eluent 3 : 1 pentane/diethyl ether) afforded pure  $L^2$  as a white solid. Yield 0.84 g, 16%. Mp 103–105 °C (lit.,<sup>17</sup> 74 °C, from a 4 : 1 mixture of  $L^2$  and  $L^3$ ). Found: C, 65.0; H, 5.5; N, 29.6%. Calcd. for  $\text{C}_{13}\text{H}_{13}\text{N}_5$ : C, 65.2; H, 5.5; N, 29.3%. Electron impact mass

spectrum  $m/z$  240  $[\text{M} + \text{H}]^+$ . NMR spectra ( $\text{CDCl}_3$ , 293 K):  $^1\text{H}$  (250 MHz):  $\delta$ , ppm 8.42 (d, 2H, 2.5 Hz, Pz  $H^5$ ), 7.70–7.88 (m, 3H, Py  $H^{3-5}$ ), 6.25 (d, 2H, 2.5 Hz, Pz  $H^4$ ), 2.38 (s, 6H,  $\text{CH}_3$ ).  $^{13}\text{C}\{^1\text{H}\}$  (63 MHz):  $\delta$ , ppm 151.9 (2C, Py  $\text{C}^{2/6}$ ), 149.9 (2C, Pz  $\text{C}^3$ ), 141.0 (1C, Py  $\text{C}^4$ ), 127.6 (2C, Pz  $\text{C}^5$ ), 108.4 and 108.0 (both 2C, Py  $\text{C}^{3/5}$  and Pz  $\text{C}^4$ ), 13.9 (2C,  $\text{CH}_3$ ).

### Synthesis of $[\text{Fe}(\text{L}^1)_2]_{0.5}[\text{I}_3]_{1.5}$ (**1**) and $[\text{Fe}_2\text{L}^1]$

A solution of  $\text{FeI}_2 \cdot 4\text{H}_2\text{O}$  (0.25 g,  $6.6 \times 10^{-4}$  mol) and  $L^1$  (0.28 g,  $1.3 \times 10^{-3}$  mol) in MeOH (50  $\text{cm}^3$ ) was refluxed for 2 h. The resultant brown solution was filtered, and concentrated under reduced pressure to ca. 5  $\text{cm}^3$ . Slow diffusion of  $\text{Et}_2\text{O}$  vapour into the solution yielded large brown crystals of **1**, contaminated by  $[\text{Fe}_2\text{L}^1]$  as a light orange powder that could be removed by decantation. For **1**: yield 0.17 g, 57% with respect to iodine. Found C, 23.8; H, 1.5; N, 12.8; I, 56.9%. Calcd. for  $\text{C}_{22}\text{H}_{18}\text{FeI}_5\text{N}_{10}$  C, 23.7; H, 1.6; N, 12.6; I, 57.0%. Electrospray mass spectrum:  $m/z$  915  $^{56}\text{Fe}_2^{127}\text{I}_3(\text{L}^1)_2]^+$ , 435  $^{56}\text{Fe}^{127}\text{I}(\text{L}^1)(\text{NCMe})]^+$ , 394  $^{56}\text{Fe}^{127}\text{I}(\text{L}^1)]^+$ , 339  $[\text{L}^1 + ^{127}\text{I}]^+$ , 312  $^{56}\text{Fe}^{127}\text{I}(\text{L}^1)_2(\text{H}_2\text{O})]^{2+}$ , 302  $^{56}\text{Fe}^{127}\text{I}(\text{L}^1)_2]^{2+}$ , 239  $^{56}\text{Fe}(\text{L}^1)_2]^{2+}$ , 212  $[\text{L}^1 + \text{H}]^+$ . For  $[\text{Fe}_2\text{L}^1]$ : yield 0.11 g, 32%. Found C, 25.3; H, 1.7; N, 13.3; I, 47.6%. Calcd. for  $\text{C}_{11}\text{H}_9\text{FeI}_2\text{N}_5$  C, 25.4; H, 1.7; N, 13.4; I, 48.7%. Electrospray mass spectrum:  $m/z$  915  $^{56}\text{Fe}_2^{127}\text{I}_3(\text{L}^1)_2]^+$ , 435  $^{56}\text{Fe}^{127}\text{I}(\text{L}^1)(\text{NCMe})]^+$ , 394  $^{56}\text{Fe}^{127}\text{I}(\text{L}^1)]^+$ , 339  $[\text{L}^1 + ^{127}\text{I}]^+$ , 302  $^{56}\text{Fe}^{127}\text{I}(\text{L}^1)_2]^{2+}$ , 239  $^{56}\text{Fe}(\text{L}^1)_2]^{2+}$ , 212  $[\text{L}^1 + \text{H}]^+$ .

### Synthesis of $[\text{Fe}(\text{L}^1)_2][\text{Co}(\text{C}_2\text{B}_9\text{H}_{11})_2]$ (**2**)

A mixture of  $\text{FeCl}_2 \cdot 4\text{H}_2\text{O}$  (0.12 g,  $5.9 \times 10^{-4}$  mol),  $L^1$  (0.25 g,  $1.2 \times 10^{-3}$  mol) and  $\text{Ag}[\text{Co}(\text{C}_2\text{B}_9\text{H}_{11})_2]$  (1.1 g,  $2.5 \times 10^{-3}$  mol) in  $\text{MeNO}_2$  (50  $\text{cm}^3$ ) was refluxed for 1 h, affording an orange solution with a white  $\text{AgCl}$  precipitate. The solution was filtered and concentrated under reduced pressure to ca. 5  $\text{cm}^3$ . Slow diffusion of  $\text{Et}_2\text{O}$  vapour into the solution at  $-10^\circ\text{C}$  yielded orange needles of the  $\text{MeNO}_2$  solvate of **2**, which were collected and dried *in vacuo* over  $\text{P}_2\text{O}_5$ . Yield 0.31 g, 46%. Found C, 31.7; H, 5.5; N, 12.6%. Calcd. for  $\text{C}_{30}\text{H}_{62}\text{B}_6\text{Co}_2\text{FeN}_{10}$  C, 32.0; H, 5.6; N, 12.4%. Electrospray mass spectrum:  $m/z$  805  $^{56}\text{Fe}^{59}\text{Co}\{\text{C}_2^{11}\text{B}_9\text{H}_{11}\}_2(\text{L}^1)_2]^+$ , 635  $^{56}\text{Fe}^{59}\text{Co}\{\text{C}_2^{11}\text{B}_9\text{H}_{11}\}_2(\text{L}^1)(\text{NCMe})]^+$ , 594  $^{56}\text{Fe}^{59}\text{Co}\{\text{C}_2^{11}\text{B}_9\text{H}_{11}\}_2(\text{L}^1)]^+$ , 501  $^{56}\text{Fe}^{59}\text{Co}\{\text{C}_2^{11}\text{B}_9\text{H}_{11}\}_2(\text{L}^1)(\text{NCMe})_2]^{2+}$ , 460  $^{56}\text{Fe}^{59}\text{Co}\{\text{C}_2^{11}\text{B}_9\text{H}_{11}\}_2(\text{L}^1)]^{2+}$ , 239  $^{56}\text{Fe}(\text{L}^1)_2]^{2+}$ , 212  $[\text{L}^1 + \text{H}]^+$ .

### Synthesis of $[\text{Fe}(\text{L}^2)_2][\text{SbF}_6]_2$ (**3**)

A solution of  $\text{FeCl}_2 \cdot 4\text{H}_2\text{O}$  (0.12 g,  $5.9 \times 10^{-4}$  mol),  $L^2$  (0.29 g,  $1.2 \times 10^{-3}$  mol) and  $\text{AgSbF}_6$  (0.41 g,  $1.2 \times 10^{-3}$  mol) in  $\text{MeNO}_2$  (50  $\text{cm}^3$ ) was refluxed for 1 h. The resultant  $\text{AgCl}$  precipitate was removed by filtration, and the yellow solution concentrated under reduced pressure to ca. 5  $\text{cm}^3$ . Slow diffusion of  $\text{Et}_2\text{O}$  vapour into the solution gave large mustard-yellow crystals of the product, which were collected and dried *in vacuo* over  $\text{P}_2\text{O}_5$ . Yield 0.37 g, 62%. Found C, 31.1; H, 2.6; N, 14.1%. Calcd. for  $\text{C}_{26}\text{H}_{26}\text{F}_{12}\text{FeN}_{10}\text{Sb}_2$  C, 31.0; H, 2.6; N, 13.9%. Electrospray mass spectrum:  $m/z$  = 267  $^{56}\text{Fe}(\text{L}^2)_2]^{2+}$ , 240  $[\text{L}^2 + \text{H}]^+$ .  $^1\text{H}$  NMR spectrum ( $\text{CD}_3\text{CN}$ ):  $\delta$ , ppm 70.7, 67.9, 37.4 (all 4H, Py  $H^{3/5}$  and Pz  $H^4$  and  $H^5$ ), 7.1 (12H,  $\text{CH}_3$ ), 6.2 (2H, Py  $H^4$ ). Peak linewidths range between 50–70 Hz. UV/vis/NIR spectrum (MeCN, 298 K):  $\nu_{\text{max}}/10^3$   $\text{cm}^{-1}$  ( $\epsilon_{\text{max}}/\text{M}^{-1} \text{cm}^{-1}$ ) 7.1 (8.5), 9.4 (sh), 11.4 (sh), 23.4 (sh), 25.3 (sh), 26.3 (sh), 32.3 (38800), 36.4 (23400), 40.0 (70400), 41.0 (sh).

**Table 3** Experimental details for the single crystal structure determinations in this study

	1	2·CH <sub>3</sub> NO <sub>2</sub> (1/0.75)	3
Molecular formula	C <sub>22</sub> H <sub>18</sub> FeI <sub>5</sub> N <sub>10</sub>	C <sub>30.75</sub> H <sub>64.25</sub> B <sub>36</sub> Co <sub>2</sub> FeN <sub>10.75</sub> O <sub>1.5</sub>	C <sub>30.75</sub> H <sub>64.25</sub> B <sub>36</sub> Co <sub>2</sub> FeN <sub>10.75</sub> O <sub>1.5</sub>
<i>M<sub>r</sub></i>	1112.81	1171.55	1171.55
Crystal class	Monoclinic	Orthorhombic	Orthorhombic
Space group	<i>P2/c</i>	<i>Pca2<sub>1</sub></i>	<i>Pca2<sub>1</sub></i>
<i>a</i> /Å	15.9084(3)	37.297(2)	37.3516(19)
<i>b</i> /Å	13.6094(3)	10.5955(6)	10.5840(6)
<i>c</i> /Å	15.1155(2)	29.6321(17)	29.5118(15)
<i>β</i> /°	104.3473(8)	—	—
<i>V</i> /Å <sup>3</sup>	3170.50(10)	11710.1(12)	11666.9(11)
<i>Z</i>	4	8	8
<i>T</i> /K	150(2)	300(2)	150(2)
<i>μ</i> (Mo-Kα)/mm <sup>-1</sup>	5.375	0.847	0.850
Measured reflections	41942	146512	105918
Independent reflections	7248	18205	22460
<i>R<sub>int</sub></i>	0.154	0.039	0.059
<i>R</i> ( <i>F</i> ) <sup>a</sup>	0.049	0.044	0.077
<i>wR</i> ( <i>F</i> <sup>2</sup> ) <sup>b</sup>	0.133	0.117	0.214
Goodness of fit	1.068	1.051	1.078
Flack parameter	—	0.496(11)	0.49(2)

$$^a R = \sum [|F_o| - |F_c|] / \sum |F_o|, ^b wR = [\sum w(F_o^2 - F_c^2) / \sum wF_o^4]^{1/2}.$$

### Single crystal X-ray structure determinations

Crystals of **1** were grown by slow diffusion of Et<sub>2</sub>O vapour into a solution of the compound in methanol, while crystals of **2·CH<sub>3</sub>NO<sub>2</sub>** and **3** were similarly grown from MeNO<sub>2</sub>/Et<sub>2</sub>O. Experimental data from these structure determinations are collected in Table 3. Diffraction data from **1** and **3** were collected on a Nonius KappaCCD area detector diffractometer, using graphite-monochromated Mo-Kα radiation ( $\lambda = 0.71073$  Å) from a sealed tube source. Since crystals of **2·CH<sub>3</sub>NO<sub>2</sub>** diffract weakly, data from this compound were obtained using a Bruker X8 Apex diffractometer, with graphite-monochromated Mo-Kα radiation generated by a rotating anode. Both diffractometers are fitted with Oxford Cryostream low temperature devices. All structures in this study were solved by direct methods (*SHELXS96*<sup>29</sup>), and developed by full least-squares refinement on *F*<sup>2</sup> (*SHELXL96*<sup>30</sup>). All crystallographic figures were prepared using *XSEED*,<sup>31</sup> which incorporates *POVRAY*.<sup>32</sup>

Experimental details for the structure determinations of [Fe(L<sup>2</sup>)<sub>2</sub>][BF<sub>4</sub>]<sub>2</sub>·4CH<sub>3</sub>CN and [Fe(L<sup>2</sup>)<sub>2</sub>][ClO<sub>4</sub>]<sub>2</sub>·(CH<sub>3</sub>)<sub>2</sub>CO are given in the ESI.†

CCDC reference numbers 278897–278908.

For crystallographic data in CIF or other electronic format see DOI: 10.1039/b510370c

**Single crystal X-ray structure of [Fe(L<sup>1</sup>)<sub>2</sub>][I<sub>0.5</sub>][I<sub>3</sub>]<sub>1.5</sub> (**1**).** The asymmetric unit of this compound contains one complex dication lying on a general position; one half-occupied iodide anion lying on the *C*<sub>2</sub> axis (1, *y*, 0.75); two half-occupied triiodide anions lying on *C*<sub>2</sub> axes (0.5, *y*, 0.75) and (0.5, *y*, 0.25); and a disordered half-occupied triiodide ion lying across the *C*<sub>2</sub> axis (0, *y*, 0.25). The disordered half-anion was modelled over two equally occupied sites, with I–I bonds that were restrained to 2.92(2) Å. All non-H atoms were refined anisotropically, and all H atoms were placed in calculated positions and refined using a riding model. Two residual Fourier peaks of 1.0–1.7 e Å<sup>-3</sup>, and the deepest Fourier hole of -2.3 e Å<sup>-3</sup>, are all <1 Å from an I atom. There is a third residual

Fourier peak of 1.1 e Å<sup>-3</sup>, lying 2.5 Å from two I atoms of the same I<sub>3</sub><sup>-</sup> half-anion.

**Single crystal X-ray structure of [Fe(L<sup>1</sup>)<sub>2</sub>][Co(C<sub>2</sub>B<sub>9</sub>H<sub>11</sub>)<sub>2</sub>]<sub>2</sub>·CH<sub>3</sub>NO<sub>2</sub>(1/0.75) (2·CH<sub>3</sub>NO<sub>2</sub> (1/0.75)).** The same crystal was used for data collection at 150 and 300 K. The crystal diffracted weakly at 300 K, and data were only collected to  $2\theta = 47.9^\circ$ . The crystal diffracted more strongly at 150 K, allowing data to  $2\theta = 53.7^\circ$  to be obtained. The precision of the refinement at 150 K is noticeably inferior to the 300 K structure, however, which may reflect lattice strain and/or unresolved disorder induced by the partial spin-transition undergone by the crystal upon cooling. Although the *Pca2<sub>1</sub>* space group adopted by the compound is polar, the crystal used was a racemic twin, with both hands equally populated according to its Flack parameter (which is 0.5 within experimental error). The asymmetric unit contains two complex dications, four cobalticborane anions and two nitromethane molecules. The latter were modelled at both temperatures with occupancies of 0.9 and 0.6. This gives a total solvent content of 1.5 molecules per asymmetric unit, or 0.75 per formula unit, in the crystal examined.

At 300 K both solvent sites are disordered over two positions, with occupancy ratios of 0.5 : 0.4 and 0.3 : 0.3 respectively. These were modelled using the restraints C–N = 1.45(2), N–O = 1.15(2), C...O = 2.30(2) and O...O = 1.88(2) Å. All non-H atoms except for the disordered solvent were refined anisotropically, and all H atoms were placed in calculated positions and refined using a riding model. There is one notable residual Fourier peak of 1.27 e Å<sup>-3</sup>, located 1.0 Å from Fe(1A).

At 150 K only one orientation of each solvent site was detected, although discrepancies in their C–N and N–O bond lengths imply that there may also be some unresolved disorder at these temperatures. All non-H atoms except for the 60% occupied solvent site were refined anisotropically, and all H atoms were placed in calculated positions and refined using a riding model. One carbaborane C atom became non-positive definite during the refinement process, and was restrained so that its individual

thermal parameters approximate to isotropic behaviour during the final least squares cycles with a *SHELXL* ISOR instruction. There are three residual Fourier peaks of 1.7–2.2 e Å<sup>-3</sup>, each ≤ 1.1 Å from one of the metal atoms in the model.

**Single crystal X-ray structure of [Fe(L<sup>2</sup>)<sub>2</sub>][SbF<sub>6</sub>]<sub>2</sub>(3).** No disorder was detected during refinement of this structure, and no restraints were applied to it. All non-H atoms were refined anisotropically, while H atoms were placed in calculated positions and refined using a riding model. The deepest Fourier hole of -1.4 e Å<sup>-3</sup> is 0.9 Å from one of the antimony atoms.

### Other measurements

UV/vis spectra were obtained with a Perkin-Elmer Lambda 900 spectrophotometer, operating between 100–200 nm, in 1 cm quartz cells. Electron impact and electrospray (MeCN matrix) mass spectra were respectively performed with VG AutoSpec and Micromass LCT TOF spectrometers. CHN microanalyses were performed by the University of Leeds School of Chemistry microanalytical service. NMR spectra were run on a Bruker ARX250 spectrometer, operating at 250.1 MHz (<sup>1</sup>H) or 62.9 MHz (<sup>13</sup>C). Magnetic susceptibility measurements were obtained using a Quantum Design SQUID magnetometer in an applied field of 1000 G. Diamagnetic corrections were estimated from Pascal's constants.<sup>20</sup> Theoretical fits of the susceptibility data to the equation for the zero-field splitting of a high-spin d<sup>6</sup> transition ion<sup>20,21</sup> were carried out using *SIGMAPLOT*.<sup>33</sup>

### Acknowledgements

The authors thank Dr H. J. Blythe (University of Sheffield) for the susceptibility data, and the EPSRC and the University of Leeds for funding.

### References

- 1 J. A. Real, A. B. Gaspar and M. C. Muñoz, *Dalton Trans.*, 2005, 2062.
- 2 M. A. Halcrow, *Coord. Chem. Rev.*, 2005, DOI: 10.1016/j.ccr.2005.03.010.
- 3 J. M. Holland, J. A. McAllister, Z. Lu, C. A. Kilner, M. Thornton-Pett and M. A. Halcrow, *Chem. Commun.*, 2001, 577.
- 4 J. M. Holland, J. A. McAllister, C. A. Kilner, M. Thornton-Pett, A. J. Bridgeman and M. A. Halcrow, *J. Chem. Soc., Dalton Trans.*, 2002, 548.
- 5 V. A. Money, I. Radosavljevic Evans, M. A. Halcrow, A. E. Goeta and J. A. K. Howard, *Chem. Commun.*, 2003, 158.
- 6 J. M. Holland, S. A. Barrett, C. A. Kilner and M. A. Halcrow, *Inorg. Chem. Commun.*, 2002, 5, 328.
- 7 V. A. Money, J. Elhaik, M. A. Halcrow and J. A. K. Howard, *Dalton Trans.*, 2004, 1516.
- 8 V. A. Money, J. S. Costa, S. Marcén, G. Chastanet, J. Elhaik, M. A. Halcrow, J. A. K. Howard and J.-F. Létard, *Chem. Phys. Lett.*, 2004, 391, 273.
- 9 J. Elhaik, C. A. Kilner and M. A. Halcrow, *CrystEngComm*, 2005, 7, 151.
- 10 J. Elhaik, D. J. Evans, C. A. Kilner and M. A. Halcrow, *Dalton Trans.*, 2005, 1693.
- 11 J. Elhaik, V. A. Money, S. A. Barrett, C. A. Kilner, I. Radosavljevic Evans and M. A. Halcrow, *Dalton Trans.*, 2003, 2053.
- 12 V. A. Money, I. Radosavljevic Evans, J. Elhaik, M. A. Halcrow and J. A. K. Howard, *Acta Crystallogr., Sect. B*, 2004, 60, 41.
- 13 V. A. Money, J. Elhaik, I. Radosavljevic Evans, M. A. Halcrow and J. A. K. Howard, *Dalton Trans.*, 2004, 65.
- 14 C. A. Kilner and M. A. Halcrow, *Polyhedron*, 2005, DOI: 10.1016/j.poly.2005.06.034.
- 15 See e.g., T. Buchen, P. Gülich and H. A. Goodwin, *Inorg. Chem.*, 1994, 33, 4573; T. Buchen, P. Gülich, K. H. Sugiyarto and H. A. Goodwin, *Chem. Eur. J.*, 1996, 2, 1134; S. Marcén, L. Lecren, L. Capes, H. A. Goodwin and J.-F. Létard, *Chem. Phys. Lett.*, 2002, 358, 87; K. H. Sugiyarto, W.-A. McHale, D. C. Craig, A. D. Rae, M. L. Scudder and H. A. Goodwin, *Dalton Trans.*, 2003, 2443; A. Bhattacharjee, V. Ksenofontov, K. H. Sugiyarto, H. A. Goodwin and P. Gülich, *Adv. Funct. Mater.*, 2003, 13, 877.
- 16 D. L. Jameson and K. A. Goldsby, *J. Org. Chem.*, 1990, 55, 4992.
- 17 X. Sun, Z. Yu, S. Wu and W.-J. Xiao, *Organometallics*, 2005, 24, 2959.
- 18 F. Calderazzo, U. Englert, C. Hu, F. Marchetti, G. Pampaloni, V. Passarelli, A. Romano and R. Santi, *Inorg. Chim. Acta*, 2003, 344, 197.
- 19 A. R. Karam, E. L. Catari, F. López-Linares, G. Agrifoglio, C. L. Albano, A. Diaz-Barrios, T. E. Lehmann, S. V. Pekarar, L. A. Albornoz, R. Atencio, T. Gonzalez, H. B. Ortega and P. Joskowics, *Appl. Catal., A*, 2005, 280, 165.
- 20 C. J. O'Connor, *Prog. Inorg. Chem.*, 1982, 29, 203.
- 21 R. Boča, *Coord. Chem. Rev.*, 2004, 248, 757.
- 22 See e.g., S. Calogero, G. G. Lobbia, P. Cecchi, G. Valle and J. Friedl, *Polyhedron*, 1994, 13, 87; J. Kusz, H. Spiering and P. Gülich, *J. Appl. Crystallogr.*, 2001, 34, 229 and refs. therein; G. Psomas, N. Brefuel, F. Dahan and J.-P. Tuchagues, *Inorg. Chem.*, 2004, 43, 4590.
- 23 See e.g., D. L. Reger, C. A. Little, V. G. Young, Jr. and M. Pink, *Inorg. Chem.*, 2001, 40, 2870.
- 24 See e.g., P. Guionneau, J.-F. Létard, D. S. Yufit, D. Chasseau, G. Bravic, A. E. Goeta, J. A. K. Howard and O. Kahn, *J. Mater. Chem.*, 1999, 9, 985; A. F. Stassen, M. de Vos, P. J. van Koningsbruggen, F. Renz, J. Ensling, H. Kooijman, A. L. Spek, J. G. Haasnoot, P. Gülich and J. Reedijk, *Eur. J. Inorg. Chem.*, 2000, 2231.
- 25 See e.g., M. S. Haddad, W. D. Federer, M. W. Lynch and D. N. Hendrickson, *J. Am. Chem. Soc.*, 1980, 102, 1468; N. Moliner, A. B. Gaspar, M. C. Muñoz, V. Niel, J. Cano and J. A. Real, *Inorg. Chem.*, 2001, 40, 3986.
- 26 L. Pauling, *The Nature of the Chemical Bond*, Cornell University Press, Ithaca NY, USA, 3rd edn, 1960, pp. 257–264.
- 27 P. H. Svensson and L. Klöo, *Chem. Rev.*, 2003, 103, 1649.
- 28 Z. Xie, T. Jelinek, R. Bau and C. A. Reed, *J. Am. Chem. Soc.*, 1994, 116, 1907.
- 29 G. M. Sheldrick, *Acta Crystallogr., Sect. A*, 1990, 46, 467.
- 30 G. M. Sheldrick, *SHELXL97, Program for the refinement of crystal structures*, University of Göttingen, Germany, 1997.
- 31 L. J. Barbour, *J. Supramol. Chem.*, 2003, 1, 189.
- 32 *POVRAY* v. 3.5, Persistence of Vision Raytracer Pty. Ltd., Williamstown, Victoria, Australia, 2002, <http://www.povray.org>.
- 33 *SIGMAPLOT*, v. 8.02, SPSS Scientific Inc., Chicago IL, 2002.